Sixth International Symposium on Turbulence and Shear Flow Phenomena
Seoul, Korea, 22-24 June 2009

NUMERICAL INVESTIGATION OF SHOCK WAVE AND TURBULENT BOUNDARY LAYER INTERACTION ON AN AIRFOIL

Li-Wei Chen, Chang-Yue Xu, and Xi-Yun Lu
Department of Modern Mechanics,
University of Science and Technology of China
Hefei, Anhui 230026, China
xlu@ustc.edu.cn

ABSTRACT

Shock wave and turbulent boundary layer interaction on an 18% thick circular-arc airfoil was studied numerically using detached-eddy simulation for a free-stream Mach number $M_\infty = 0.76$ and a Reynolds number $Re = 1.1 \times 10^7$. Results have been validated carefully against experimental data. Based on the flow characteristics, three typical flow regimes are classified as attached boundary layer, moving shock wave/turbulent boundary layer interaction, and intermittent boundary layer separation region. The turbulent statistical quantities have been analyzed in detail and different behaviors are found in the three flow regimes. Some quantities, e.g. pressure-dilatation correlation and dilatational dissipation, have exhibited that the compressibility effect is enhanced due to the shock wave/boundary layer interaction. The results obtained in this study provide a physical insight into the understanding of the mechanisms underlying in this complex flow.

INTRODUCTION

Owing to the obvious importance in a wide range of fundamentals and applications, a great effort has been made in the past decades to study the compressible flow in transonic regime past an airfoil. Self-sustained shock wave motions on airfoils have been investigated experimentally and numerically (e.g. Lee 2001 and references cited there). Previous experimental studies of transonic flow over an 18% thick circular-arc airfoil at zero incidence have indicated that upstream propagating shock waves occur alternately on the upper and lower surfaces for a certain range of the free-stream Mach number (McDevitt et al., 1976; Levy, 1978; McDevitt, 1979; Marvin et al., 1980), which belongs to the type C (Tijdeman and Seebass, 1980). Moreover, some numerical simulations have been performed using the time-dependent two-dimensional Reynolds-averaged Navier-Stokes (RANS) equations with turbulence models (Marvin et al., 1980; Rumsey et al., 1996). A zonal detached-eddy simulation method has also been used to predict the buffet phenomenon on a supercritical airfoil (Deck, 2005). Those simulations have analyzed the shock wave motion and the evolution of the shock-induced separation.

The interaction between the sustained moving shock wave and turbulent boundary layer interaction along the airfoil surface is an important issue on understanding the flow characteristics. Smits and Dussauge (1996) have classified the shock wave/turbulent boundary layer interactions as compression corner interactions or incident shock interactions. Numerical investigations have been performed for the compression corner interactions (e.g. Loginov et al., 2006) or incident shock interactions (e.g. Pirozzoli and Grasso, 2006). Andreopoulos et al. (2000) have analyzed several types of shock/turbulence interactions and concluded that in the case of wall-bounded interactions the shock system is highly unsteady. Correspondingly, the flow considered here involves complex interaction phenomena and turbulent boundary layer behaviors related to the shock wave motion and the surface curvature of the airfoil. The relevant study comparably is scarce.

The present work investigates the compressible flow past an 18% thick circular-arc airfoil for a free-stream Mach number $M_\infty = 0.76$ and a Reynolds number $Re = 1.1 \times 10^7$. The three-dimensional Favre-averaged compressible Navier-Stokes equations are solved numerically by means of a finite-volume approach (Lu et al., 2005) combining with shock capture technique (Hill et al., 2006). As the Reynolds number is high, the detached-eddy simulation is implemented for turbulence closure (Simon et al., 2007; Spalart, 2009). The motivation of this work is to study various fundamental mechanisms dictating the complex flow phenomena.

MATHEMATICAL FORMULATION AND METHOD

Three-dimensional Favre-averaged compressible Navier-Stokes equations in generalized coordinates are employed. To non-dimensionalize the equations, we use the free-stream variables including the density ρ_∞, temperature T_∞, speed of sound a_∞, and chord of the airfoil c as characteristic scales. A detailed description of the mathematical formulation can be found in our previous paper (e.g. Lu et al., 2005). The initial condition is set as the free-stream quantities. The far field boundary conditions are treated by local one-dimensional Riemann-invariants. No-slip and adiabatic conditions are applied on the airfoil surface. Periodic condition is used in the spanwise direction of the airfoil.

Detached-eddy simulation is implemented in the present work for turbulence closure (Spalart, 2009). The model is derived from the Spalart-Allmaras (SA) model, which is a one-equation model for the eddy viscosity $\tilde{\nu}$ by solving a transport equation, referred to the original paper (Spalart and Allmaras, 1992) for details on the constants and the quantities involved.

The model is provided with a destruction term for the eddy viscosity that depends on the distance to the nearest solid wall d. This term adjusts the eddy viscosity $\tilde{\nu}$ to scale with local deformation rate $\tilde{S}$ producing an eddy viscosity given by $\tilde{\nu} \sim \tilde{S}d^2$. Spalart et al. (1997) proposed to replace d to the closest wall with $\tilde{d}$ defined by $\tilde{d} = \min(d, C_{DES}\Delta)$, where Δ represents a characteristic mesh length and the constant C_{DES} is taken as 0.65 (Shur et al., 1999).

The governing equations are numerically solved by the finite-volume method. The temporal integration is performed using an implicit approximate-factorization method

with sub-iterations to ensure the second-order accuracy. Both the convective and diffusive terms are discretized with second-order centered schemes, and a fourth-order low artificial numerical dissipation is employed to prevent numerical oscillations (Lu et al., 2005). A binary sensor function is used to detect the discontinuity caused by shock waves (Hill et al., 2006). Then, the second-order Roe's flux-difference splitting will be activated for capturing shock wave.

COMPUTATIONAL OVERVIEW AND VALIDATION

Computational overview

We consider a compressible flow past an 18% thick circular-arc airfoil at zero incidence with the free-stream Mach number $M_\infty = 0.76$ and the Reynolds number based on the chord of the airfoil equal to 1.1×10^7. The C-type 3D grid contains $522 \times 192 \times 82$ with the width of spanwise $0.4c$. The time step is $0.001c/a_\infty$, proved to be small enough in predicting the present unsteady flow. The computed time elapses to about $400c/a_\infty$ to obtain statistically meaningful turbulence properties in the temporal averaging operation.

The present code is equipped with a multi-block domain decomposition feature to facilitate parallel processing in a distributed computing environment (Lu et al., 2005). The present computational domain is divided into 32 subdomains for parallel processing.

The averaging procedure in postprocess is based on resolved quantities such as, density $\bar{\rho}$, pressure $\bar{p}$, temperature $\tilde{T}$, and velocity $\tilde{u}_i$, where a tilde denotes the Favre filter. $\langle\ \rangle$ means the average in time (after careful elimination of the transient part of their time-dependent variations) and in the spanwise direction, and $\{\phi\} = \langle\bar{\rho}\phi\rangle/\langle\bar{\rho}\rangle$ with a variable ϕ. Then, their fluctuations are obtained as (Garnier et al., 2002) $\rho' = \bar{\rho} - \langle\bar{\rho}\rangle$, $p' = \bar{p} - \langle\bar{p}\rangle$, $T'' = \tilde{T} - \{\tilde{T}\}$, and $u_i'' = \tilde{u}_i - \{\tilde{u}_i\}$, respectively.

Validation

Figure 1 shows the profile of average pressure $\langle C_p\rangle$ coefficient. The result appears to compare favourably with the experimental data (McDevitt et al., 1976). Figure 2 shows the transverse distributions of the averaged streamwise velocity and shear stress at some typical measurement locations $x/c = 0.8$ and 0.90, where z^* is the relative transverse coordinate defined as $z^* = z - z_s$ with z_s being the transverse location of the airfoil surface. Reasonable agreement is obtained with the experimental measurements of (Marvin et al., 1980).

Moreover, the present numerical strategy has already been applied with success to a wide range of turbulent flows such as the compressible turbulent swirling flows injected into a coaxial dump chamber (Lu et al., 2005) and compressible flows over a circular cylinder (Xu et al., 2009). We have carefully examined the physical model and numerical approach used in this study and verified the calculated results are reliable.

RESULTS AND DISCUSSION

Flow structures and shock wave motions

Figure 3 depicts the coherent structures educed by isosurface of the Q criterion (Jeong and Hussain, 1995). The shock wave shape is reasonably visualized by the surface of density gradient, suggesting that the deformation of shock

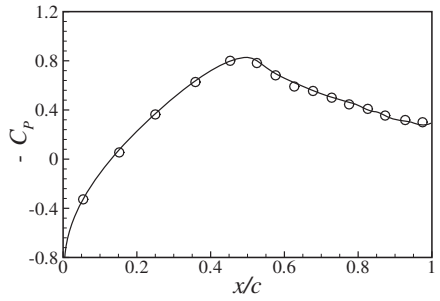

Figure 1: Distribution of time-averaged pressure coefficient, where solid line represents computational result and symbol experimental data (McDevitt *et al.* 1976).

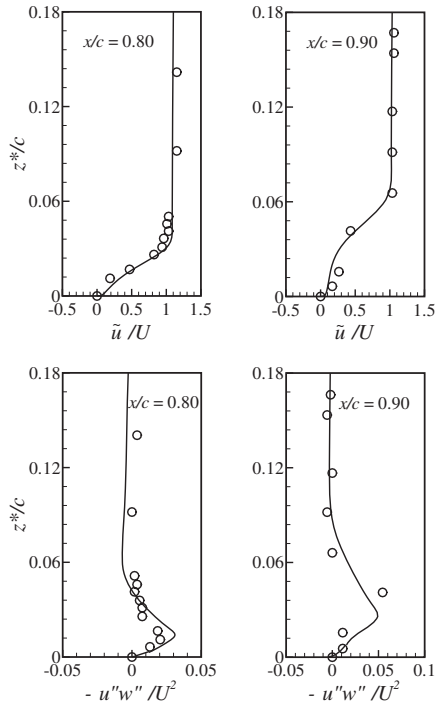

Figure 2: Transverse distributions of mean streamwise velocity and shear stress obtained numerically and experimentally, where solid line represents computational result and symbol experimental data (Marvin *et al.* 1980).

wave shape along the spanwise direction is negligibly small even near turbulent boundary layer. As shown in figures 3(a)-3(b), the boundary layer separation is induced by the strong moving shock wave. The separated free shear layer roll up and becomes the 3D complex structures due to the vortical instability as the shear layer evolves downstream. The streamwise vortical structures become strengthened in the near wake. In figures 3(c)-3(d), the shock wave weakens as it approximates at the mid-chord and the shock-induced separation disappears nearly.

To illustrate the unsteady features of the flow, figure 4 shows the time development of flow structures using the isocontours of $\|\nabla\bar{\rho}\|$, for clarity, in the mid-span (x, z) plane. Here, we pay our attention on flow evolution over the upper surface. A series of compression waves develop in the region near the trailing-edge and move upstream to coalesce into a strong shock wave at $x/c = 0.83$ approximately. This

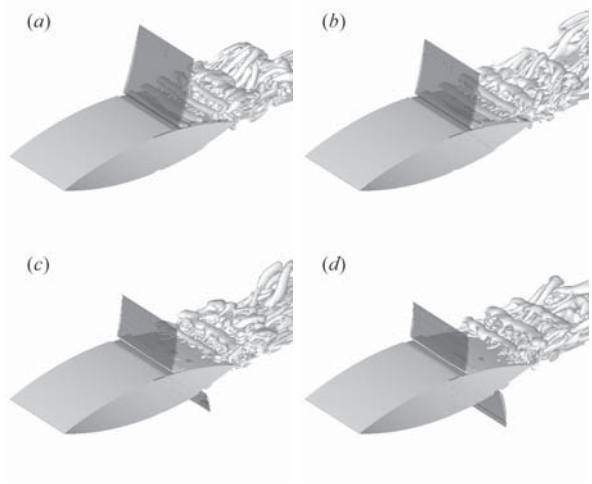

Figure 3: Shock-induced separated coherent structures educed by iso-surface of the Q-criterion at $Q = 10(U_\infty/c)^2$ with the same time increment from (a) to (d). The surface of shock wave is exhibited by $\|\nabla\bar{\rho}\| = 10(\rho_\infty/c)$.

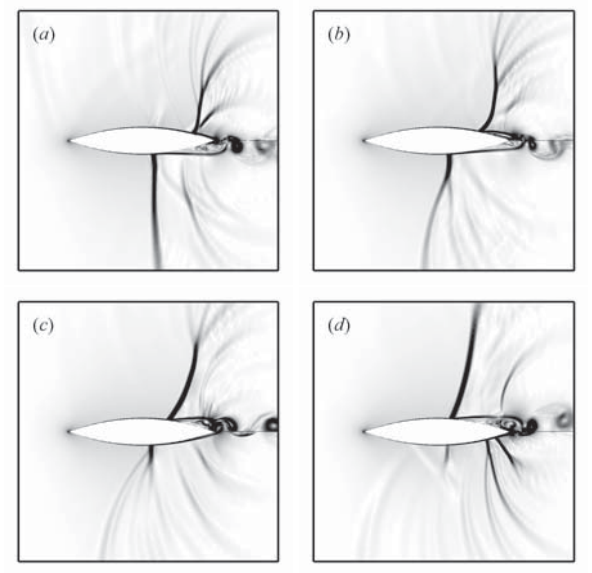

Figure 4: Numerical schlieren-like visualization by iso-contours of $\|\bar{\rho}\|$ in the mid-span plane during half period with the same time increment from (a) to (d).

shock wave moves upstream while increasing its strength, and induces the boundary layer separation. Then, the shock wave weakens again to be weak shock wave or compression wave around the mid-chord. Further, the compression wave continues its upstream motion, leaves the airfoil from the leading-edge, and propagates upstream into the oncoming flow. Meanwhile, the compression wave diffraction at the top of shock wave reasonably occurs. As a symmetrical airfoil is considered, this phenomenon is repeated alternately between the upper and lower surfaces.

From the preceding description on the shock wave evolution, it is reasonably identified that the shock wave motion belongs to the type C classified by Tijdeman and Seebass (1980), which is also confirmed by the previous experiments (McDevitt et al., 1976; Marvin et al.,1980). To determine the frequency of the shock wave motion, the power spectrum density is obtained from the time-dependent lift force exerting on the airfoil. The primary frequency corresponding to the highest peak is $St = 0.148$ approximately, or the reduced frequency, $k = \pi St \approx 0.465$, consistent well with the previous experimental data $0.44 \sim 0.49$ (e.g. McDevitt et al., 1976; Levy, 1978; Marvin et al., 1980).

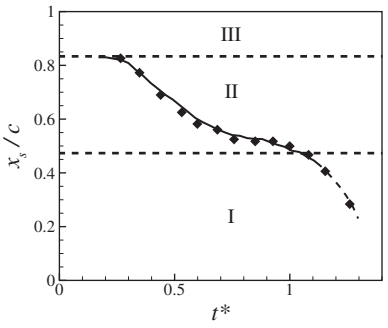

Figure 5: Variation of shock location, where solid (shock wave) and dashed (compression wave) lines represent computational result and symbol experimental data (McDevitt 1979). Region I denotes attached boundary layer, II moving shock wave/turbulent boundary layer interaction, and III intermittent boundary layer separation.

The location of shock wave motion along the surface is shown in figure 5, where t^* represents the fractional cyclic time during one period and $t^* = 0$ is taken as the time when the shock wave is at the mid-chord of the airfoil (McDevitt, 1979). Reasonable agreement is obtained with the experimental measurements (McDevitt, 1979). As the shock wave moves upstream shown in figure 4, the shock wave weakens and even becomes compression wave, represented by the dashed line in figure 5. When the compression wave propagates upstream further and leaves the airfoil from the leading-edge, it is difficult to identify the compression wave position, which does not show for $x/c < 0.2$ in figure 5.

Turbulent boundary layer characteristics

Division of flow regions. To clearly present the physical mechanisms underlying in this flow, we may classify three typical flow regions, including attached boundary layer (or neatly expressed as region I), moving shock wave/turbulent boundary layer interaction (II), and intermittent boundary layer separation (III), respectively. The regions along the airfoil surface are shown schematically in figure 5. The shock wave motion is characterized in the region of $0.47 < x/c < 0.83$ approximately. The attached and intermittently separated boundary layer regions lie from the leading-edge to $x/c = 0.47$ and from $x/c = 0.83$ to the trailing-edge, respectively. In this section, we will discuss and compare the turbulent boundary layer characteristics in these three regions.

Mean velocity profiles. The comparison of the mean streamwise velocity predicted numerically with experimental data (Marvin et al., 1980) has been shown in figure 2 and reasonable agreement is found. To deal with the mean velocity profiles in different regions, figure 6 shows the transverse distributions of the mean streamwise velocity. In the region I, i.e. $x/c = 0.2$ and 0.4, we identify that the van Dri-

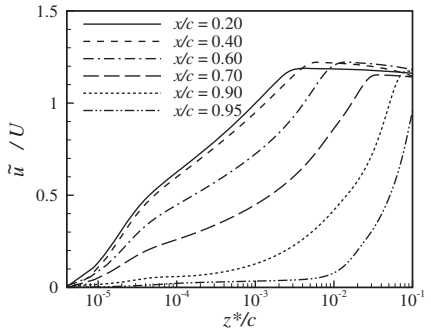

Figure 6: Distributions of mean streamwise velocity at various streamwise locations.

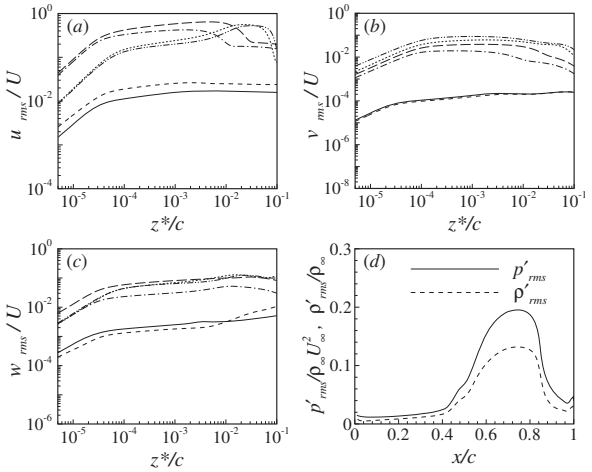

Figure 7: Distributions of turbulence intensities along the transverse direction at various streamwise locations $(a)-(c)$ (the legend is referred to figure 6) and pressure and density fluctuations along the surface (d).

est transformed mean velocity profiles, obtained as defined by (Bradshaw, 1977) and scaled by the wall-friction velocity, agree well with the linear and logarithmic law of the wall, though favorable pressure gradient occurs from figure 1. In the region II, i.e. $x/c = 0.6$ and 0.7, due to the shock wave/boundary layer interaction, the velocity profiles exhibit a linear behavior approximately in the viscous sublayer and no longer obey the logarithmic law. As the boundary layer separation occurs intermittently in the region III, the mean streamwise velocity exhibits small value in the near region of the surface.

Turbulence intensities. Figure 7 shows the transverse distributions of the normalized turbulence intensity components. The streamwise component in figure $7(a)$ dominates the turbulence intensity as expected, compared with other two components in figures $7(b)$ and $7(c)$. This character is consistent with measurements (McDevitt et al., 1976; Marvin et al., 1980). Here, we mainly pay our attention on the behaviors in the three flow regimes.

One of the major features of shock wave/turbulence interactions is the amplification of turbulence intensities which is a direct effect of the Rankine-Hugoniot relations (Andreopoulos et al., 2000). As shown in figures $7(a)$-$7(c)$, the turbulence intensities in the region II, such as at $x/c = 0.6$ and 0.7, are enhanced significantly compared to those at $x/c = 0.2$ and 0.4, consistent with the results of the experimental measurements (McDevitt et al., 1976; Marvin et al., 1980). Here, we introduce the turbulence Mach number defined as $M_t = \{u_i'' u_i''\}^{\frac{1}{2}}/a_{loc}$ (Lele, 1992) and have identified that the M_t reaches as high as 0.5 approximately in the region II. Thus, the effect of the moving shock wave on turbulence intensities must be considered. As the turbulent normal stress is increased across a shock, the propagation speed of the shock wave is slightly faster to bring about a specified compression based on the shock-jump relations in a turbulent flow (Lele, 1992). This specified compression is an additional mechanism to enhance the turbulence intensities in the region II, compared to the compression corner shock interactions (Loginov et al., 2006) and incident shock interactions (Pirozzoli and Grasso, 2006).

We further discuss the turbulence intensities in the region III, as shown in figures $7(a)$-$7(c)$ at $x/c = 0.9$ and 0.95. Compared to the region II, the streamwise turbulence intensity component near the surface reduces in figure $7(a)$ and the spanwise component somewhat enhances in figure $7(b)$. This behavior is associated with the development of vortical structures over the surface. As shown in figure 3, the separated shear layer induced by shock wave rolls up. Then, the spanwise vortical structures become unstable and the streamwise vortices strengthen gradually, resulting in the increase of the spanwise velocity fluctuation.

The distributions of the normalized pressure and density fluctuations along the surface are also shown in figure $7(d)$. The fluctuations are significantly enhanced in the region II, consistent with the turbulence intensities. The profiles exhibit a sharp change at $x/c = 0.83$ approximately, corresponding to the initial shock wave location coalesced by a series of upstream propagating compression waves from the trailing-edge region shown in figure 4.

Turbulent kinetic energy and budget terms

Turbulent kinetic energy. The specific turbulent kinetic energy, $k = \{u_i'' u_i''\}/2$, shown in figure 8 is significantly enhanced in the region II. As noticed in the incident shock wave/boundary layer interaction (Pirozzoli and Grasso, 2006), a spatially evolving turbulent compressible boundary layer exhibits close similarities with the incompressible case. The turbulent kinetic energy for incompressible boundary layers obeys the near-wall asymptotic behavior (Patel et al., 1985; Speziale et al., 1992),

$$k \simeq A_k z^{*2}, \tag{1}$$

where A_k is a constant. In the present study, the profiles in figure 8 satisfy (1) well in the viscous sublayer. The turbulent flow in the three regions exhibits the similar asymptotic behavior with different values of the constant A_k; a large value of A_k occurs in the region II. Downstream of the interaction region, turbulence satisfies the asymptotic consistency with different values of the constant A_k and experiences a relaxation toward an equilibrium state.

Budget terms in the turbulent kinetic energy transport equation. The budget terms in the turbulent kinetic energy transport equation, which have been given in detail by Shyy and Krishnamurty (1997), are discussed. Figure $9(a)$ shows the transverse distributions of the turbulent kinetic energy production term due to the mean velocity gradient

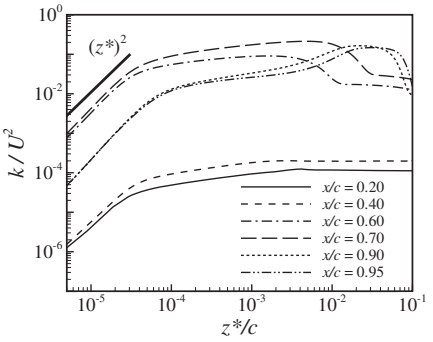

Figure 8: Distribution of specific turbulent kinetic energy at various streamwise locations.

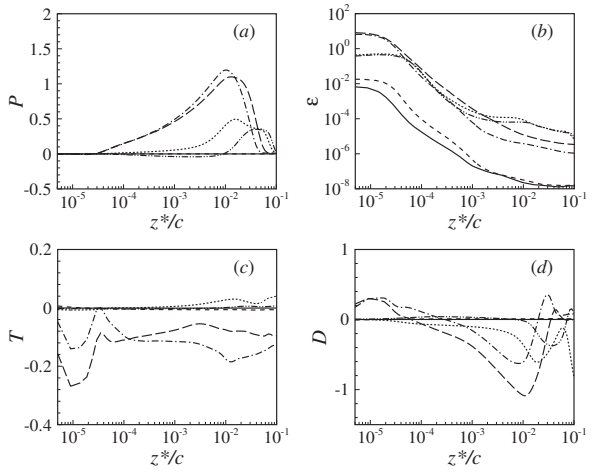

Figure 9: Transverse distributions of turbulent kinetic energy budget terms at various streamwise locations: (a) turbulent kinetic energy production, (b) turbulent dissipation rate, (c) pressure-dilatation, (d) turbulent diffusion. The legend is referred to figure 8.

$P = -\langle\bar{\rho}u_i''u_j''\rangle\{\tilde{u}_i\}_{,j}$. The production is very small in the region I such as at $x/c = 0.2$ and 0.4, corresponding to the weak turbulent kinetic energy in figure 8. In the region II, the production significantly strengthens due to the moving shock wave/boundary layer interaction. Then, the production in the region III gradually decreases and its peak location corresponds to the strongest shear layer, as seen from the profiles at $x/c = 0.9$ and 0.95.

The profiles of the turbulent dissipation term $\epsilon = \langle\tau_{ij}''u_{i,j}''\rangle$ are shown in figure 9(b). The strong dissipation occurs in the region II as expected. Similar to the analysis for the near-wall asymptotic behavior (1), turbulent dissipation also obeys the near-wall relation (Patel et al., 1985; Speziale et al., 1992), i.e. $\epsilon \simeq 2A_k + B_\epsilon z^*$ with B_ϵ being a constant and nearly zero (Pirozzoli and Grasso, 2006). It is observed that the profiles follow this relation well in the viscous sublayer in figure 9(b).

Figure 9(c) shows the pressure-dilatation correlation term $T = \langle p'u_{j,j}''\rangle$, which is an important compressibility term in the turbulent kinetic energy budget (Sarkar, 1992). This correlation is weak in the regions I and III, while its distributions around -0.15 appear at $x/c = 0.6$ and 0.7, which are reasonably associated with the shock wave motion and result in turbulence decay due to the compressibility effect.

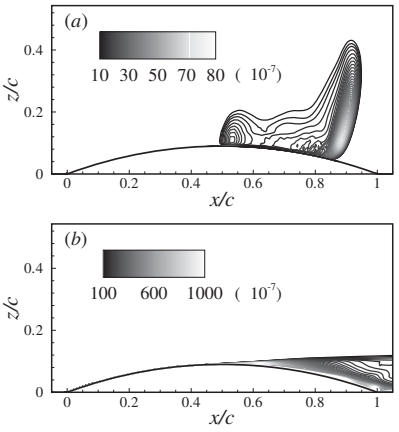

Figure 10: Distributions of the turbulent dissipation rate decomposition: (a) dilatational part ϵ_d; (b) solenoidal part ϵ_s.

The distributions of turbulent diffusion term, $D = -\langle\bar{\rho}u_i''u_i''u_j''/2 + p'u_i''\delta_{ij}\rangle_{,j}$, are shown in figures 9$(d)$. The turbulent flow undergoes a decay process, especially in the region II, and the process goes slowly in the region III.

We further examine the effect of moving shock wave on the turbulent dissipation rate ϵ, which can be separated into a solenoidal part ϵ_s and a dilatational part ϵ_d (Zeman, 1990; Sakar et al., 1991),

$$\begin{aligned}\epsilon =&\langle\tau_{ij}''u_{i,j}''\rangle\\ =&\langle\frac{\tilde{\mu}}{Re}\omega_i''\omega_i'' + 2\frac{\tilde{\mu}}{Re}(u_{i,j}''u_{j,i}'' - (u_{i,i}'')^2)\rangle\\ &+\frac{4}{3}\langle\frac{\tilde{\mu}}{Re}(u_{i,i}'')^2\rangle\\ =&\epsilon_s + \epsilon_d,\end{aligned} \tag{2}$$

where ω_i'' denotes the fluctuating vorticity vector. The isocontour lines of both the parts are shown in figure 10. The dilatational part is a pure compressibility effect. The dilatational part shown in figure 10(a) obviously occurs in the region II, especially around the region where a series of compression waves coalesce to form a strong shock wave. The solenoidal part in figure 10(b) mainly exists in the near wall region and in the wake. The dilatational dissipation is enhanced by the moving shock wave, but it remains smaller compared to the total turbulent dissipation rate, consistent with the results of the confined three-dimensional turbulent mixing layer with shocks (Vreman et al., 1995).

CONCLUDING REMARKS

Numerical investigation on the compressible flow past an airfoil was carried out by means of a detached-eddy simulation technique. Self-sustained shock wave motions repeated alternately along the upper and lower surfaces of the airfoil are reasonably identified, which belong to the type C classified by Tijdeman and Seebass (1980) and agree with the previous experimental findings (McDevitt et al., 1976; Levy, 1978; McDevitt, 1979; Marvin et al., 1980).

As the substantial unsteadiness of moving shock wave on the airfoil, we may classify three typical flow regimes including attached boundary layer, moving shock wave/turbulent boundary layer interaction, and intermittent boundary layer separation region. Turbulent boundary layer characteristics in terms of mean velocity, turbulence intensities, tur-

bulent kinetic energy, and the relevant turbulent quantities have been analyzed in detail in the three flow regions. The turbulence intensities are significantly enhanced with a strengthened turbulent kinetic energy production induced by the moving shock wave. The pressure-dilatation correlation term related to the compressibility effect is relatively important in the shock wave/boundary layer interaction region and reasonably decays turbulence. Moreover, as the turbulent dissipation rate can be separated into solenoidal and dilatational part, it is identified that the dilatational dissipation is enhanced by the moving shock wave but remains smaller, and the solenoidal dissipation exists in the near wall region and in the wake.

ACKNOWLEDGMENTS

This work was supported by the National Natural Science Foundation of China (Nos. 90405007 and 10832010) and the Innovative Foundation of the Chinese Academy of Sciences (Nos. KJCX2-YW-L05 and CXJJ-237).

REFERENCES

Andreopoulos, Y., Agui, J. H., and Briassulis, G., 2000, "Shock wave-turbulence interactions", *Annual Review of Fluid Mechanics*, Vol. 32, pp. 309-345.

Bradshaw, P., 1977, "Compressible turbulent shear layers", *Annual Review of Fluid Mechanics*, Vol. 9, pp. 33-54.

Deck, S., 2005, "Numerical simulation of transonic buffet over a supercritical airfoil", *AIAA Journal*, Vol. 43, pp. 1556-1566.

Garnier, E., Sagaut, P., and Deville, M., 2002, "Large eddy simulation of shock/homogeneous turbulence interaction", *Computers & Fluids*, Vol. 31, pp. 245-268.

Hill, D. J., Pantano, C., and Pullin, D. I., 2006, "Large-eddy simulation and multiscale modelling of a Richtmyer-Meshkov instability with reshock", *Journal of Fluid Mechanics*, Vol. 557, pp. 29-61.

Jeong, J., and Hussain, F., 1995, "On the identification of a vortex", *Journal of Fluid Mechanics*, Vol. 285, pp. 69-94.

Lee, B. H. K., 2001, "Self-sustained shock oscillations on airfoils at transonic speeds", *Progress in Aerospace Science*, Vol. 37, pp. 147-196.

Lele, S. K., 1992, "Shock-jump relations in a turbulent flow", *Physics of Fluids A*, Vol. 4, pp. 2900-2905.

Levy, L. L., 1978, "Experimental and computational steady and unsteady transonic flows about a thick airfoil", *AIAA Journal*, Vol. 16, pp. 564-572.

Loginov, M. S., Adams, N. A., and Zheltovodov, A. A., 2006, "Large-eddy simulation of shock-wave/turbulent-boundary-layer interaction", *Journal of Fluid Mechanics*, Vol. 565, pp. 135-169.

Lu, X. Y., Wang, S. W., Sung, H. G., Hsieh, S. Y., and Yang, V., 2005, "Large-eddy simulations of turbulent swirling flows injected into a bump chamber", *Journal of Fluid Mechanics*, Vol. 527, pp. 171-195.

Marvin, J. G., Levy, L. L., and Seegmiller, H. L., 1980, "Turbulence modeling for unsteady transonic flows", *AIAA Journal*, Vol. 18, pp. 489-496.

McDevitt, J. B., 1979, "Supercritical flow about a thick circular-arc airfoil", *NASA Tech. Mem.* 78549.

McDevitt, J. B., Levy, L. L., and Deiwert, G. S., 1976, "Transonic flow about a thick circular-arc airfoil", *AIAA Journal*, Vol. 14, pp. 606-613.

Patel, V. C., Rodi, W., and Scheuerer, G., 1985, "Turbulence models for near-wall and low Reynolds number flows: a review", *AIAA Journal*, Vol. 23, pp. 1308-1319.

Pirozzoli, S., and Grasso, F., 2006, "Direct numerical simulation of impinging shock wave/turbulent boundary layer interaction at M=2.25", *Physics of Fluids*, Vol. 18, 065113.

Rumsey, C. L., Sanetrik, M. D., Biedron, R. T., Melson, N. D., and Parlette, E. B., 1996, "Efficiency and accuracy of time-accurate turbulent Navier-Stokes computations", *Computers & Fluids*, Vol. 25, pp. 217-236.

Sarkar, S., 1992, "The pressure-dilatation correlation in compressible flows", *Physics of Fluids A*, Vol. 4, pp. 2674-2682.

Sarkar, S., Erlebacher, G., Hussaini, M. Y., and Kreiss, H. O., 1991, "The analysis and modelling of dilatational terms in compressible turbulence", *Journal Fluid Mechanics*, Vol. 227, pp. 473-493.

Shur, M. L., Spalart, P. R., Strelets, M., and Travin, A., 1999, "Detached-eddy simulation of an airfoil at high angle of attack," *4th International Symposium on Engineering Turbulence Modelling and Experiments*, W. Rodi and D. Laurence, ed., Elsevier, Amsterdam, Vol. 4, pp. 669-678.

Shyy, W., and Krishnamurty, V. S., 1997, "Compressible effects in modeling complex turbulent flows", *Progress in Aerospace Science*, Vol. 33, pp. 587-645.

Simon, F., Deck, S., Guillen, P., Sagaut, P., and Merlen, A., 2007, "Numerical simulation of the compressible mixing layer past an axisymmetric trailing edge", *Journal of Fluid Mechanics*, Vol. 591, pp. 215-253.

Smits, A. J., and Dussauge, J. P., 1996, *Turbulent Shear Layers in Supersonic Flow*, American Institute of Physics, Melville, NY.

Spalart, P. R., 2009, "Detached-eddy simulation", *Annual Review of Fluid Mechanics*, Vol. 41, pp. 181-202.

Spalart, P. R., and Allmaras, S. R., 1992, "A one-equation turbulence model for aerodynamic flows", *AIAA paper* 92-0439.

Spalart, P. R., Jou, W. H., Strelets, M., and Allmaras, S. R., 1997, "Comments on the feasibility of LES for wings and on a hybrid RANS/LES approach," *Proceedings of the 1st AFOSR International Conference on DNS/LES*, C. Liu and Z. Liu, ed., Greyden, Columbus, OH.

Speziale, C. G., Abid, R., and Anderson, E. C., 1992, "Critical evaluation of two-equation models for near-wall turbulence", *AIAA Journal*, Vol. 30, pp. 324-331.

Tijdeman, H., and Seebass, R., 1980, "Transonic flow past oscillating airfoils", *Annual Review of Fluid Mechanics*, Vol. 12, pp. 181-222.

Vreman, B., Kuerten, H., and Geurts, B., 1995, "Shocks in direct numerical simulation of the confined three-dimensioal mixing layer", *Physics of Fluids*, Vol. 7, pp. 2105-2107.

Xu, C. Y., Chen, L. W., and Lu, X. Y., 2009, "Numerical investigation of shock wave and turbulence interaction over a circular cylinder", *Modern Physics Letter B*, Vol. 23, pp. 233-236.

Zeman, O., 1990, "Dilatation dissipation: the concept and application in modeling compressible mixing layers", *Physics of Fluids A*, Vol. 2, pp. 178-188.